JGR Solid Earth

RESEARCH ARTICLE
10.1029/2021JB022314

Key Points:
- A stacked spectral ratio approach can separate depth dependence of source and path effects
- Analyses of spectral decomposition inversions suggest that previous reports of increase in stress drop with depth may be overstated
- Source parameter analyses should explicitly include depth-dependent attenuation models or empirical corrections

Supporting Information:
Supporting Information may be found in the online version of this article.

Correspondence to:
R. E. Abercrombie,
rea@bu.edu

Citation:
Abercrombie, R. E., Trugman, D. T., Shearer, P. M., Chen, X., Zhang, J., Pennington, C. N., et al. (2021). Does earthquake stress drop increase with depth in the crust? *Journal of Geophysical Research: Solid Earth*, *126*, e2021JB022314. https://doi.org/10.1029/2021JB022314

Received 4 MAY 2021
Accepted 14 SEP 2021

Does Earthquake Stress Drop Increase With Depth in the Crust?

Rachel E. Abercrombie[1], Daniel T. Trugman[2], Peter M. Shearer[3], Xiaowei Chen[4], Jiewen Zhang[4], Colin N. Pennington[4,5], Jeanne L. Hardebeck[5], Thomas H. W. Goebel[6], and Christine J. Ruhl[7]

[1]Department of Earth and Environment, Boston University, Boston, MA, USA, [2]Jackson School of Geosciences, University of Texas at Austin, Austin, TX, USA, [3]Scripps Institution of Oceanography, University of California San Diego, La Jolla, CA, USA, [4]School of Geosciences, The University of Oklahoma, Norman, OK, USA, [5]USGS, Earthquake Science Center, Moffett Field, CA, USA, [6]Center for Earthquake Research and Information, University of Memphis, Memphis, TN, USA, [7]Department of Geosciences, The University of Tulsa, Tulsa, OK, USA

Abstract We combine earthquake spectra from multiple studies to investigate whether the increase in stress drop with depth often observed in the crust is real, or an artifact of decreasing attenuation (increasing Q) with depth. In many studies, empirical path and attenuation corrections are assumed to be independent of the earthquake source depth. We test this assumption by investigating whether a realistic increase in Q with depth (as is widely observed) could remove some of the observed apparent increase in stress drop with depth. We combine event spectra, previously obtained using spectral decomposition methods, for over 50,000 earthquakes (M0 to M5) from 12 studies in California, Nevada, Kansas and Oklahoma. We find that the relative high-frequency content of the spectra systematically increases with increasing earthquake depth, at all magnitudes. By analyzing spectral ratios between large and small events as a function of source depth, we explore the relative importance of source and attenuation contributions to this observed depth dependence. Without any correction for depth-dependent attenuation, we find a systematic increase in stress drop, rupture velocity, or both, with depth, as previously observed. When we add an empirical, depth-dependent attenuation correction, the depth dependence of stress drop systematically decreases, often becoming negligible. The largest corrections are observed in regions with the largest seismic velocity increase with depth. We conclude that source parameter analyses, whether in the frequency or time domains, should not assume path terms are independent of source depth, and should more explicitly consider the effects of depth-dependent attenuation.

Plain Language Summary The stress release (or stress drop) during an earthquake provides information about the energy budget, and the slip and area of rupture, which are needed to investigate earthquake triggering and rupture dynamics. Stress drop is also an important element of seismic hazard forecasting since high stress drop earthquakes radiate more high frequency energy, resulting in stronger ground shaking. As depth increases in the earth, the stress on faults increases because of the increased weight of the rocks above. Therefore, many models predict that deeper earthquakes should have higher stress drops. Deeper earthquakes radiate more high frequency energy than shallow ones, and some studies have interpreted this as an increase in stress drop with depth. However, attenuation of seismic energy as the waves travel through the earth is also depth-dependent, and this is rarely explicitly included in analyses. We perform a combined analysis of frequency spectra from over 50,000 previously studied earthquakes. We compare ratios of large to small magnitude earthquakes, from different depth ranges, to separate the effects of depth-dependent source radiation from depth-dependent attenuation. We find that depth-dependent attenuation can have a first-order effect and account for much of the previously reported apparent increase in stress drop with depth.

1. Introduction

The stress release, or stress drop, during earthquake rupture has long been thought to be directly related to the magnitude of the ambient stress (e.g., Byerlee & Brace, 1968; Scuderi et al., 2016; Sibson, 1974). For example, in a rate-and-state frictional model of earthquake rupture, stress drop is a function of the normal stress, and also any changes in frictional effects with slip velocity (e.g., Dieterich, 1979; Marone, 1998). The normal stress dependence is of particular interest because it implies that earthquake stress drop should increase linearly with depth throughout the seismogenic crust, and so is quantifiable (e.g., Sibson, 1974; Zoback & Harjes, 1997). Determining whether earthquake stress drop really increases with depth in the crust is hard because of the large uncertainties in stress drop measurements; some studies have reported an increase (e.g., Boyd et al., 2017; Hardebeck & Aron, 2009; Huang et al., 2017; Trugman, 2020) and others have not (e.g., Allmann & Shearer, 2007; Shearer et al., 2006). The depth dependence of the source radiation also has implications for seismic hazard; Parker et al. (2020) found that the intensity-based stress drops and peak ground accelerations of the deeper aftershocks of the 2019 Ridgecrest earthquake are underpredicted by existing ground motion equations.

Seismic moment is proportional to slip multiplied by the area of rupture, and so combining measured seismic moment with an estimate of the rupture dimension (and hence area) allows calculation of the slip, and thus the strain and stress release. To resolve spatial and depth variation of source parameters within the crust, we must use the more numerous smaller earthquakes (<M4 or M5). For these earthquakes, source dimension is estimated from the source duration (e.g., Mori et al., 2003), or by modeling the spectral shape (e.g., Brune, 1970) and so assumptions of both geometry (typically circular) and rupture velocity (typically constant or linearly increasing with depth) are required for stress drop calculations (e.g., Kaneko & Shearer, 2015).

As seismic velocities increase with depth in the earth, it seems reasonable that the rupture velocity would do the same, perhaps as a relatively constant fraction of the shear wave velocity. Marty et al. (2019) found both the release in stress and the rupture velocity to increase with confining stress in laboratory models. Studies of stress drop as a function of depth usually investigate whether reasonable increases in rupture velocity with depth are sufficient to explain any apparent trend; for example, Shearer et al. (2006) and Allmann and Shearer (2007) found that the expected rupture velocity increase was sufficient to compensate for any apparent increase in stress drop, whereas Huang et al. (2017), Boyd et al. (2017), and Hardebeck and Aron (2009) found the increase in stress drop they observed to be too large to be an artifact of increasing rupture velocity.

Unfortunately, both the rupture dimension and stress drop of small earthquakes are very hard to measure, largely because of the difficulty of removing the effects of propagation through the earth from the recorded seismograms (see Abercrombie, 2021 for a review). The attenuation structure of the earth is not sufficiently well known at the relatively high frequencies needed to resolve small earthquake source parameters, and so empirical Green's function (EGF) approaches have become popular for isolating the source radiation (e.g., Abercrombie et al., 2017; Mori & Frankel, 1990; Ross et al., 2017). Source parameters obtained in this way are thought to be the most reliable, but they can still be subject to large uncertainties and trade-offs due to the limited frequency range of the signal, as well as the simplifying model assumptions (e.g., Abercrombie, 2015, 2021; Shearer et al., 2019; Yoshimitsu et al., 2019). These problems affect both time and frequency domain analyses, and the availability of an appropriate EGF event also severely limits the number of earthquakes that can be analyzed in this manner.

Prieto et al. (2004) and Shearer et al. (2006) introduced the spectral decomposition approach as a relatively data-driven, model-independent method of obtaining consistent source parameter measurements for large numbers of small earthquakes. This approach has since been used in many other studies, with various adaptations and variations, to look for spatial and temporal variation in earthquake source parameters (e.g., Chen & Shearer, 2011; Hardebeck & Aron, 2009; Trugman, 2020; Trugman & Shearer, 2017). The underlying separation of source, path and site effects is similar to that in other generalized inversion schemes (e.g., Bindi, Spallarossa, et al., 2020; Oth et al., 2011), but they differ in how they remove site effects that are common to all stations. Shearer et al. (2019) demonstrated how trade-offs between parameters remain a serious problem in large scale inversion studies, because of the limited frequency bandwidth available. They also concluded that relative parameters were better resolved than absolute values, a finding supported by the comparative analysis of Pennington et al. (2021).

The spectral decomposition and generalized inversion approaches are powerful as they use recordings from large numbers of earthquakes and stations to increase stability, but in doing so significant simplifications are required to constrain the number of unknown parameters. The parametrization of attenuation and estimation of site effects used in these approaches implicitly assume that the attenuation experienced depends only on the travel time from source to receiver, and is independent of the source depth of each earthquake. Complementary inversions, that make simplifying assumptions about the source to focus on the attenuation structure (e.g., Eberhart-Phillips, 2016; Hauksson & Shearer, 2006), often find that Q increases, and attenuation strongly decreases, with depth, as observed in deep boreholes (e.g., Abercrombie, 1997). These results are consistent with earlier work by Hough and Anderson (1988) that showed significant depth variation of Q in the crust. If Q increases significantly with depth, then the attenuation experienced by waves from a deeper earthquake could be significantly less than that experienced by waves from a shallower earthquake over the same length of travel time (apart from localized site effects). Ignoring this could potentially lead to a depth-dependence in attenuation being interpreted as a depth dependence in stress drop.

A few studies have investigated explicitly including depth-dependent attenuation in the inversions (e.g., Edwards & Rietbrock, 2009; Edwards et al., 2008), finding that it can compensate for the depth increase in stress drop which results from assuming attenuation is independent of source depth. Most studies have preferred a simpler parametrization where attenuation depends only on travel time, to minimize the number of free parameters in the inversion (e.g., Bindi, Spallarossa, et al., 2020; Shearer et al., 2006). Goertz-Allmann and Edwards (2014) compared the two approaches, and found that they needed to include frequency-dependent Q to obtain agreement, under the assumption of attenuation independent of earthquake source depth. Including depth-dependent attenuation in the inversion was able to compensate for the depth increase in stress drop observed without it. However, they did not investigate the effects of explicitly including depth-dependent Q in the spectral decomposition approach.

Here, we compile event spectra from previous studies and analyze them systematically to investigate whether we can distinguish between depth-dependent source and path effects. Our goal is to determine whether previously reported increases in stress drop with depth could be an artifact of failing to correct fully for depth-dependent Q. We do not attempt to calculate absolute stress drop estimates in all the different regions. We begin by describing the event spectra that form the basis of our analysis, and the velocity models that we use. We then relate our investigation of the depth dependence of spectral shape, and how we use spectral ratios between different sets of earthquakes in specific magnitude and depth ranges to distinguish between source and path effects. We find that a significant amount of previously reported increase in stress drop with depth is an artifact of assuming no change in attenuation with depth.

2. Event Spectra From Previous Spectral Decomposition Analysis

2.1. Theoretical Background to Calculation of Event Spectra

We analyze the event spectra calculated following the general spectral decomposition method introduced by Prieto et al. (2004) and Shearer et al. (2006) in the 12 studies listed in Table 1. The event spectra obtained by this method are essentially the relative source spectra, averaged over all stations, after correcting for path and site terms. At each available station, the amplitude spectrum of a time window of approximately 1 s (depends on the study) containing the direct P wave from an earthquake is calculated and compared to a similar spectrum of a preceding noise window. If the signal is larger than the noise by some threshold in the required frequency range, then the spectrum is included in the decomposition analysis. Details of the precise parameter values and thresholds are given in the original studies.

The aim of spectral decomposition is to isolate the contributions of the source, path and site effects in the recorded spectra, taking advantage of the fact that stacking (or averaging) large numbers of spectra will compensate for uncertainties from irregularities in individual observations. Each spectrum ($X_{ij}(f)$) from source i, recorded at station j can be considered a product of the source, path and site effects:

$$X_{ij}(f) = e_i(f) \times s_j(f) \times t_{k(i,j)}(f) \times r_{ij} \tag{1}$$

where the site effect at a station ($s_j(f)$) is common to all events, $t_{k(i,j)}(f)$ is the travel-time dependent path effect over path k, the event term ($e_i(f)$) includes the source and any site or local path effects common to all stations, and r_{ij} is the residual. The travel time term ($t_{k(i,j)}(f)$) is typically discretized into 1 s increments of travel time. Equation 1 is typically solved using a robust least-squares approach that varies by study, iteratively solving for $s_j(f)$, $t_{k(i,j)}(f)$, and $e_i(f)$, minimizing r_{ij}.

10.1029/2021JB022314

Table 1
Information for the Data Sets Used From the Spectral Decomposition Studies

ID	Name	Reference	Number of events	M_L range	M_w range	Shallow and deep ranges[a] (km)	Low f for Mo: Hz (samples)	f range for fitting (Hz)	Velocity model
Ha-H	Hayward Fault—on Hayward fault only	Hardebeck and Aron (2009)	984	1–4.2	1.4–4.0	<6 & 8–13	3.9–7.8 Hz (3–5)	3.9–40[b]	Hardebeck and Aron (2009)—each side of fault
Li-T	Bay Area Livermore Basin[c]	Trugman and Shearer (2018)	1622	1.5–4.2	1.9–3.9	<6 & 10–24	2.5–4 Hz (5–7)	2.5–25	SF CVM[d]
SF-T	Bay Area SAF and HF[c]	Trugman and Shearer (2018)	3037	1.5–4.3	1.7–3.9	<5 & 8–22	2.5–4 Hz (5–7)	2.5–25	SF-CVM[d]
Pf-Z	Parkfield, San Andreas Fault	Zhang et al. (2019)	4454	0–3	0.9–3.4	<4.5 & 8–15	2–4 Hz (55–80)	2–60	Thurber et al. (2006) 1D approximations of each side of fault
Mo-R	Mogul, NV	Ruhl and Abercrombie. (2020).	4938	0–5.1	0.6–4.9	<3 & 4.2–6.5	2.5–4 Hz (5–7)	1.3–26	Ruhl et al. (2016)
La-S	Landers cluster	Shearer *et al.* (2019)	4729	0–4.4	0.3–4	<5 & 10–26	2.5–4 Hz (5–7)	1.3–25	SCEC CVM-H15.1[e]
La-T	Landers aftershocks	Trugman and Shearer (2017)	2673	1.1–4.3	1.7–4.1	<3 & 6–15	2.5–4 Hz (5–7)	2.5–25	SCEC CVM-H15.1[e]
HM-T	Hector Mine aftershocks	Trugman and Shearer (2017)	2128	1.1–4.4	1.8–4.0	<3 & 4–18	2.5–4 Hz (5–7)	2.5–25	SCEC CVM-H15.1[e]
BB-T	Big Bear aftershocks	Trugman and Shearer (2017)	2949	1.1–5	1.6–5	<3 & 6–18	2.5–4 Hz (5–7)	2.5–25	SCEC CVM-H15.1[e]
SJ-T	San Jacinto Fault Trifurcation zone	Trugman and Shearer (2017)	5591	1.1–5.4	1.5–5.4	<7.5 & 10–21	2.5–4 Hz (5–7)	2.5–25	SCEC CVM-H15.1[e]
YD-T	Yuha Desert aftershocks	Trugman and Shearer (2017)	7483	1.1–5.7	1.5–5.7	<4 & 9–19	2.5–4 Hz (5–7)	2.5–25	SCEC CVM-H15.1[e]
Ri-T	Ridgecrest aftershocks	Trugman (2020)	15,671	1.3–5	1.4–4.4	0–3 & 7–14	2.5–4 Hz (6–9)	3–30	Lomax (2020)
Ka-T	Southern Kansas	Trugman et al. (2017)	4040	1.1–5.2	1.7–5.2	<4 & 6.5–11	2.5–4 Hz (5–7)	2.5–25	Rubinstein et al. (2018)
PO-P	Prague, OK	Pennington et al. (2021)	1656	-1–3.5	1.7–4.1	<4.75 & 4.75–12	1–3 Hz (28–60)	2–60	Toth et al. (2012)
GO-C	Guthrie, OK	Chen and Abercrombie (2020)	850	1–4.3	1.9–4.3	<6.6 & 6.9–26	2–2.25 Hz (64–67)	2–40	Chen (2016)
SS-C	Salton Sea Geothermal Field[c]	Chen and Shearer (2011)	1693	0.3–5.1	1.8–3.8	<4.5 & 6–8	3–5 Hz (6–8)	3–14	SCEC CVM-H15.1[e] and Chen and Shearer (2011)
BS-C	Salton Sea—Brawley seismic zone[c]	Chen and Shearer (2011)	572	1–4.2	2–3.5	<8.5 & 9–15	3–5 Hz (6–8)	3–14	SCEC CVM-H15.1[e] and Chen and Shearer (2011)
SG-G	San Gorgonio	Goebel et al. (2015)	8010	0–4	1.5–4.3	<8 & 13–24	1.6–3.1 Hz (3–5)	2–20	SCEC CVM-H15.1[e]

Note. The velocity structures are included in the Supporting Information S1. The GO-C and PO-P studies analyzed both P and S waves, but we use only the P-wave source spectra here for consistency. All are in California except where noted.

[a]The maximum depth shown is the maximum depth used for all events in the analysis. [b]Hardebeck and Aron (2009) used the frequency range 3.9–55 Hz, but we used a lower limit due to concerns about the low signal-to-noise ratio at high frequencies. [c]Sub-area polygon in Table S11. [d]SCEC Community Model (Shaw et al., 2015; Small et al., 2017). [e]SF-CVM regional 3D velocity model (Aagaard et al., 2020).

To solve Equation 1, the general spectral decomposition method assumes no source directivity, or focal mechanism corrections, and that the available stations provide a reliable average of the focal sphere (e.g., Kaneko & Shearer, 2015). At this stage in the analysis, there is no assumed spectral shape or model for any of the terms, such as a Brune source model (Brune, 1970), or exponential attenuation (e.g., Anderson & Hough, 1984). In all implementations of the spectral decomposition approach considered here, it is also assumed that $t_{k(i,j)}$ depends only on the source-receiver travel time, and is otherwise independent of the location or depth of the earthquakes; no lateral or azimuthal variations in attenuation within the study volume are considered. The calculation of independent attenuation functions for different travel-time lengths allows for differences in attenuation for longer ray paths that on average are deeper, and hence the attenuation per unit travel time is typically less for the longer travel-times (see Trugman, 2020, Figure S6, for example). This is consistent with the pattern of attenuation observed in structures in which Q increases with depth (e.g., see Figure 9a of Eberhart-Phillips, 2016). For recordings within only a few times the source depth, paths of the same travel time can be very different for deeper and shallower earthquakes. The travel-time term also contains the effects of geometrical spreading which can be distance dependent.

To extract the earthquake source spectra from the event spectra ($e_i(f)$), a further correction is needed to separate out any site and local path effects that are common to all stations. In studies following the approach of Shearer et al. (2006), this is accomplished using a global EGF or empirical correction spectrum (ECS), typically based on the assumption that the source spectrum matches the Brune source model. Other approaches (e.g., Bindi, Spallarossa, et al., 2020; Oth et al., 2011) select reference sites at which they assume there is no frequency dependent site response.

To avoid the inherent ambiguity and uncertainty in available approaches for site response correction, we design an analysis procedure that uses only relative parameters. In this way, site effects common to all events effectively cancel out and do not influence our results. Here, we analyze ratios of the event spectra of pairs of earthquakes that are the direct result of spectral decomposition following Equation 1, without applying any assumed or empirical corrections. We cannot obtain absolute parameter estimates, but we can isolate the causes of relative variation.

Each event spectrum represents an average for the earthquake over available stations at varying distances, after removal of the site and travel-time dependent terms. It is impossible to invert or model these event terms for any quantities that depend on travel time because there is no single travel time applicable to an event spectrum. Inverting for depth dependent attenuation would involve going back to the original recorded spectra and performing a new type of inversion allowing for more variation in the travel-time terms, and consequently increased free parameters, trade-offs and uncertainties. One aim of the work presented here is to determine whether such an inversion may be required in future studies, and to find the balance between potential bias from over-simplification and the lack of constraints for greater numbers of free inversion parameters.

2.2. Data

We reanalyze the event spectra obtained from 18 separate spectral decomposition inversions in 12 analyses of P-wave spectra listed in Table 1. These include regions of northern California, southern California, Nevada, Oklahoma and Kansas, and include both natural tectonic and induced seismicity (Figure 1). Table 1 also shows the varying numbers of events, their magnitude and depth ranges, and signal frequency ranges available for each individual study. Most analyses used surface recordings from regional seismic networks (typically 100 samples/s data) and temporary deployments, but the analyses by Hardebeck and Aron (2009) and Zhang et al. (2019) on the Hayward Fault and the San Andreas Fault at Parkfield, respectively, used higher frequency shallow borehole network recordings. All analyses followed the same general decomposition process based on Equation 1, except for the analysis of Landers aftershocks by Shearer et al. (2019). Their analysis of a very dense (6 km) cluster of Landers aftershocks meant that there was so little variation in travel time to each station, the $t_{k(i,j)}(f)$ term could be ignored, and the path attenuation was absorbed by the station terms, $s_j(f)$.

Following Shearer et al. (2006) and Chen and Shearer (2011), we only include event spectra calculated from at least 5 stations that meet the signal to noise threshold. As we do not include lateral variation in our

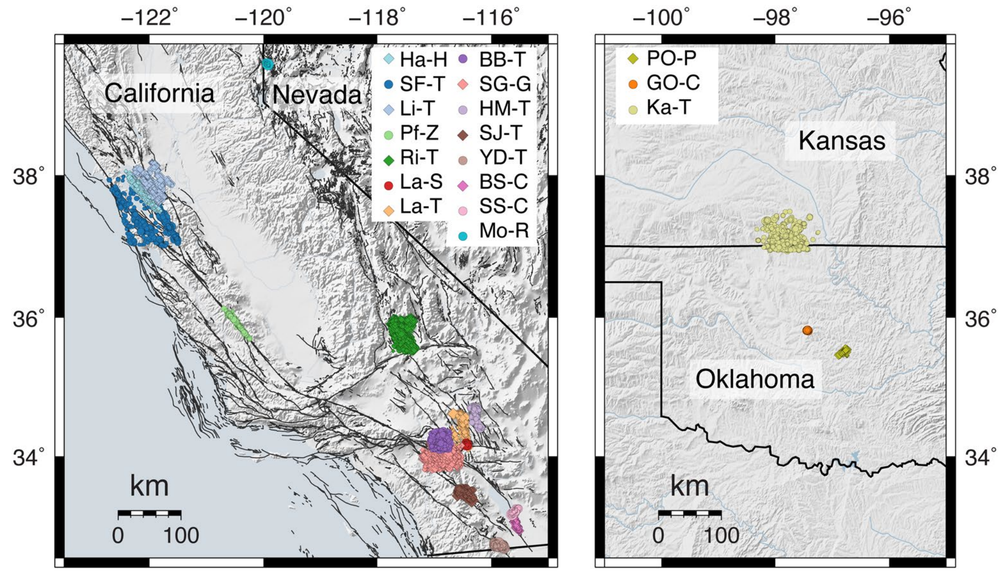

Figure 1. Maps of the earthquakes used in the analysis. See Table 1 for details, and explanation of the legend IDs.

analysis, we also subset the events from a number of studies that included distinct populations of earthquakes (Table 1); the precise area polygons are provided in the Supporting Information S1. Following the depth dependent analysis by Hardebeck and Aron (2009), we only investigate the earthquakes in their study that occurred along the Hayward Fault. We also select two sub-regions from the Bay Area analysis of Trugman and Shearer (2018), based on the SF-CVM regional 3D velocity model (Aagaard et al., 2020) to minimize the effects of lateral variations in velocity structure: one including the San Andreas and Hayward Faults, and the second in the Livermore Basin. The study of the Salton Sea region by Chen and Shearer (2011) included both shallow earthquakes related to geothermal energy production, and parts of the southern San Andreas Fault with a very different hypocentral depth distribution. We select events in these two separate regions, and also limit our analysis to earthquakes since 1989 due to changes at the time in the recording network. Chen and Shearer (2011) applied different empirical corrections to the event spectra for the pre and post 1989 earthquakes in their analysis, but as most earthquakes occurred in the later time period, and we did not want to complicate our analysis with extra corrections, we simply discarded the earlier earthquakes. For all other regions, we used all the earthquakes in the original studies that met the signal to noise criterium. The numbers of earthquakes included from each study, in each sub-region are given in Table 1, and range from 364 to 15,671, with a median of just over 2000.

For analysis of source parameters, we require consistent estimates of the earthquake magnitude; we can also use the catalog magnitudes (M_L), but they contain significant uncertainties (e.g., Pennington et al., 2021). As not all the original calculated values are available, we follow the original studies, to recalculate them. We calculate the relative amplitudes of the low frequency spectra (using the same frequency ranges as the original studies, given in Table 1). For consistency, we assume that at $M_L = 3$, $M_W = M_L$ for all regions (following Shearer et al., 2006), and so convert these relative moments into absolute estimates of seismic moment, and moment magnitude.

3. Observations of Depth Dependence to the Shape of Event Spectra

As a first step we investigate whether the frequency content of the event spectra varies consistently with hypocentral depth. All of the earthquakes considered here have been relocated using waveform cross-correlation based methods, either in the original spectral decomposition studies, or earlier, and we use these same published values (see references in Table 1). We then calculate the geometric mean amplitude of each event spectrum in both a low frequency range and a high frequency range, and calculate the ratio between these amplitudes as a measure of the spectral shapes. As the spectral shape also varies with earthquake magnitude, we plot the results in narrow magnitude bins for each region. Figure 2 shows that at all magnitudes,

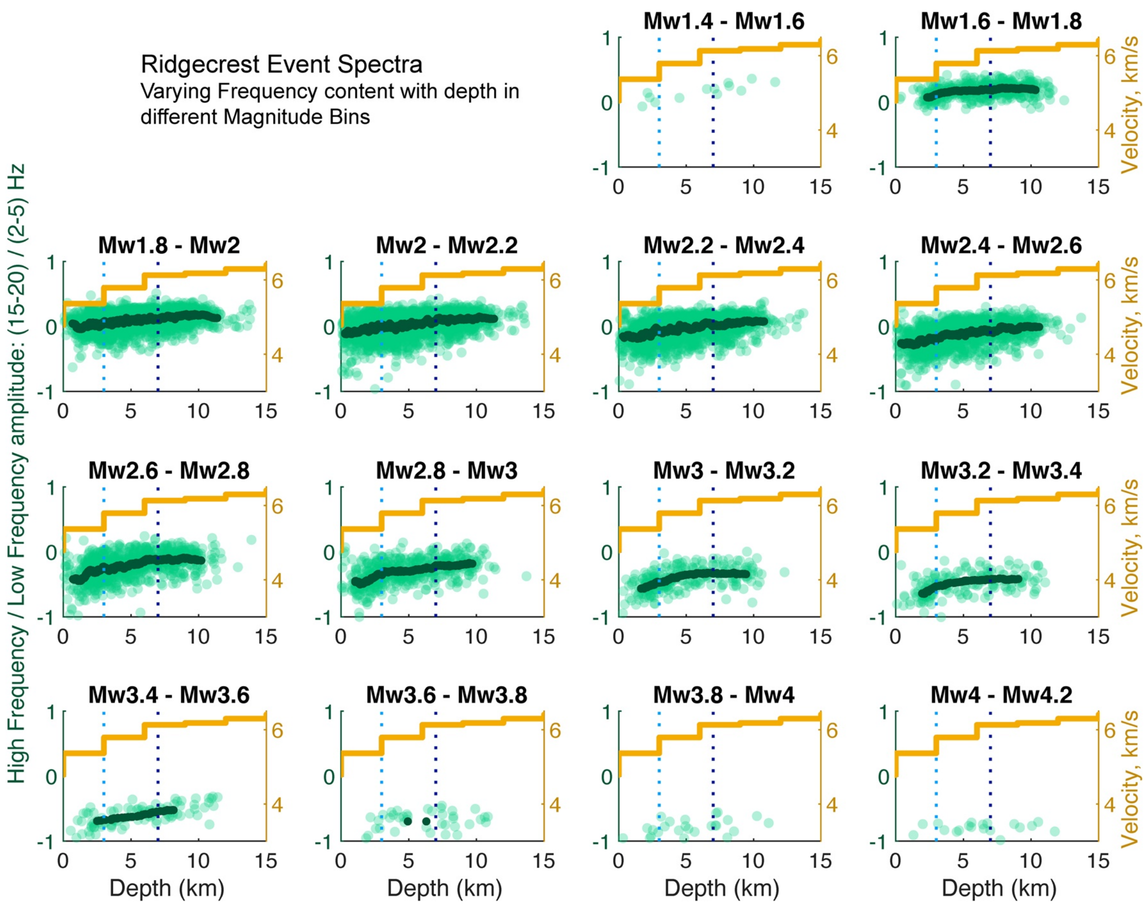

Figure 2. Ratio of high to low frequency amplitude as a function of earthquake depth for Ridgecrest aftershocks. The event spectra are divided into 0.2 Mw unit bins on the basis of their relative moments. Each log-linear plot shows the ratio of the mean high frequency (15–20 Hz) to mean low frequency (2–5.5 Hz) amplitudes of each event spectrum as a function of hypocentral depth (green circles). The running mean of 50 samples is also shown (dark green circles). The two vertical dashed lines indicate the selected cut-off depths used to determine the "deep" and "shallow" earthquakes (Table 1). The pale orange lines are the 1D velocity structure (Lomax, 2020, see Table 1). The spectra of deeper earthquakes have more high frequency energy, but this could represent either increasing stress drop with depth, or decrease in attenuation with depth.

the relative high frequency energy increases with depth for earthquakes in the Ridgecrest sequence (event spectra from Trugman, 2020). This observation is entirely consistent with the increase in stress drop with depth reported by Trugman (2020), although it is also consistent with an increase in rupture velocity with depth, a decrease in attenuation with depth, or some combination of all three. Another example is shown in the Supporting Information S1 (Figure S1). Figure 3 shows results for a single magnitude bin for all studies and sub-regions, and reveals that a similar increase in relative high frequency energy is observed in the other studies. Again, this result is consistent with the previously reported increase in stress drop with depth. These examples use binning by moment-magnitude (the number of events in each bin are shown in the Figures S2 and S3), but the results are essentially the same for local magnitude.

These systematic observations of depth dependent spectral shape could be caused by either variation in source radiation (e.g., stress drop, rupture velocity), or in attenuation, or both. Before we attempt to distinguish between these competing effects, we investigate whether there is any relationship between changes in spectral shape and local seismic velocity structure. We plot representative 1D velocity models for each region in Figures 2 and 3. These models are derived from a variety of sources, detailed in Table 1, and are selected to approximate the structure in the volume sampled by all the different ray paths from earthquakes to stations in each region. In some regions, we are able to use specific velocity models derived from local relocations and velocity inversions (e.g., Chen, 2016; Lomax, 2020; Rubinstein et al., 2018; Ruhl et al., 2016; Thurber et al., 2006; Toth et al., 2012). For other regions in Southern California we estimate the mean 1D

10.1029/2021JB022314

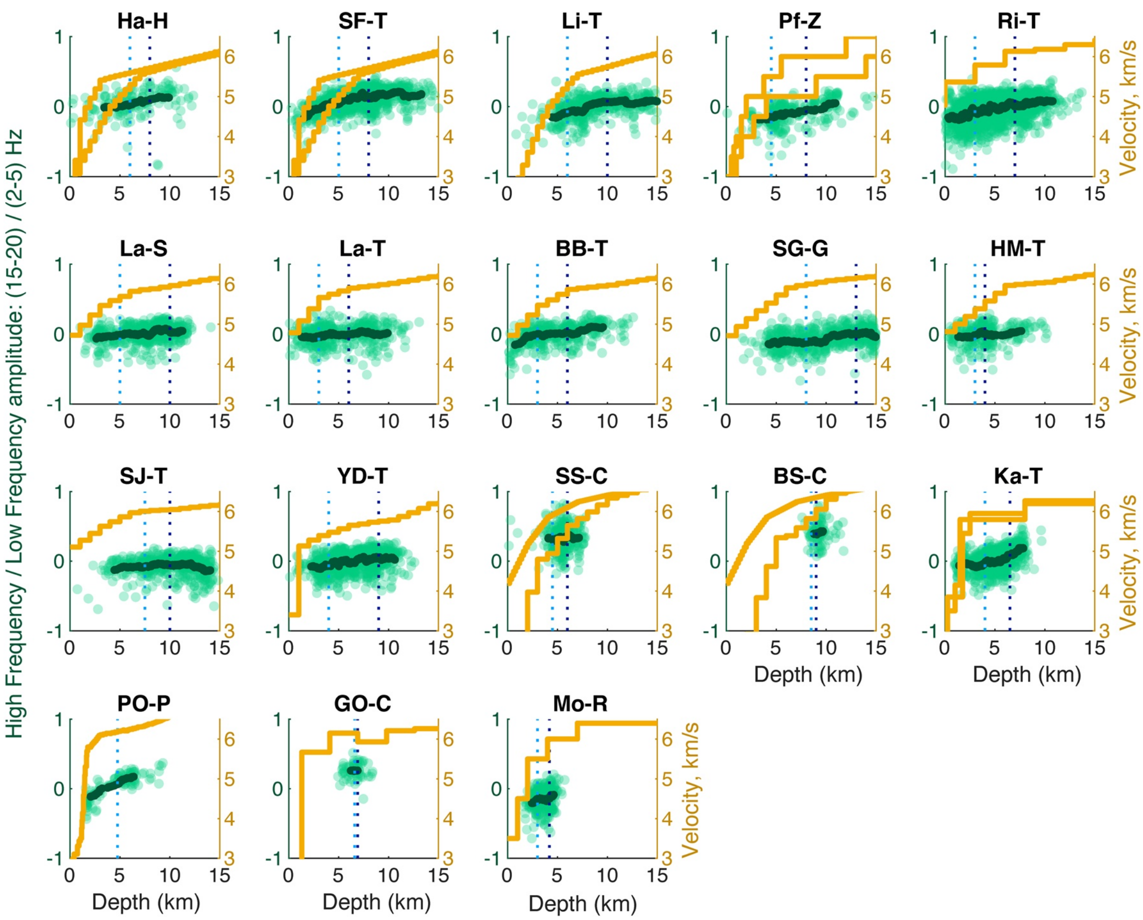

Figure 3. Ratio of high to low frequency amplitude as a function of earthquake depth for all study regions, for the example magnitude bin Mw2.2–2.4. As in Figure 2, the dark green symbols are the running means, the vertical dashed lines indicate the depths used to select the "deep" and "shallow" earthquakes in each dataset, and the orange lines are the 1D velocity structure (see Table 1 for sources). The increase in high frequency energy with depth is observed to some degree in all data sets.

velocity structure by sampling each epicentral region within the Southern California Earthquake Center (SCEC) Community Velocity Model version H15.1 (SCEC CVM-H15.1; Shaw et al., 2015) using the SCEC Unified Community Velocity Model (UCVM) software (Small et al., 2017). For the Livermore and Bay Area regions in Northern California, we similarly sample the USGS San Francisco Bay Region 3D (SF-CVM) seismic velocity model (Aagaard et al., 2020). Also, in some regions we include two models for comparison, either from similar studies (e.g., in the Salton Sea region) or for both sides of a major fault, as in the case of the Hayward fault (following Hardebeck & Aron, 2009).

A visual comparison of the variation in high frequency content of the event spectra with depth, and the representative velocity structures (Figure 3) suggests that the change in spectral shape is greater where there is greater change in velocity structure; for example, compare the Hayward Fault, Livermore and Parkfield to locations in Southern California. Kansas and Oklahoma exhibit a very rapid increase in velocity at shallow depths, but these correspond to sedimentary layers that are not sampled by many earthquakes, and so it is hard to see if there is any connection.

4. Investigation of Depth Dependent Path Effects Using Spectral Ratios

4.1. Hypothesis

The spectral decomposition analysis used to obtain the event spectra implicitly assumes that the along path attenuation is dependent only on the travel time, and so does not depend directly on the depth of the

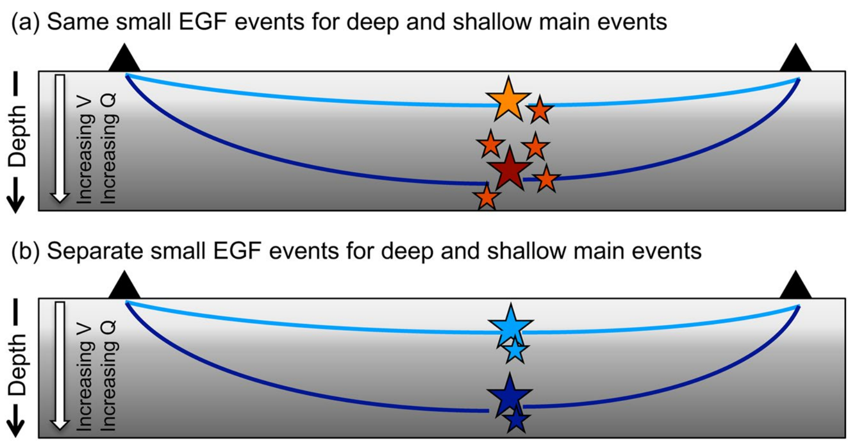

Figure 4. Cartoon Cross sections in which velocity and Q increase with depth, showing stations (black triangles), raypaths and groups of earthquakes (stars) considered. (a) Deep (dark red) and shallow (orange) larger events are corrected for attenuation using all smaller (EGF events, red), independent of depth. (b) Deep (dark blue) and shallow (pale blue) larger events are corrected for attenuation using deep (dark blue) and shallow (pale blue) EGF events, respectively. This color scheme is used throughout the paper (e.g., in Figures 5–9) for clarity.

earthquake. If Q does increase with depth, then rays with the same travel time, but from sources at different depth, could experience significantly different attenuation, as illustrated in the cartoon in Figure 4. If this depth dependence is ignored, as in spectral decomposition or analogous, generalized-inversion based approaches, then any variation in attenuation with depth will become part of the event terms, potentially appearing as a variation in stress drop with depth. In this cartoon, and in our synthetic models, we assume that the horizontal distance to the stations is greater than the focal depth, as is true for most stations used in such source parameter analyses.

We devise an EGF approach to test whether variation in attenuation with depth could explain the increase in stress drop with depth reported by a number of spectral decomposition studies. Our approach is illustrated by the cartoons in Figure 4; for each study, we consider a group of earthquakes that are shallow and another that are deep. Then we calculate spectral ratios between large and small earthquakes, assuming that the smaller events in each group serve as EGFs for the larger ones. We consider the case shown in Figure 4a where smaller earthquakes of any depth can be considered EGFs for the larger events of any depth. We compare this geometry to results where we use only smaller events of the same depth range as the larger ones Figure 4b; that is, we use only deep small events as EGFs for deep large events, and only shallow small events as EGFs for shallow large events. We refer to this geometry as using depth-specific EGFs to correct for the depth-dependent attenuation.

To demonstrate the possible outcomes, we calculate three simple, synthetic examples in Figure 5. In Figures 4 and 5, we introduce a consistent color scheme that we use throughout the paper to improve clarity. We consider the effects of either (a) attenuation decreasing (Q increasing) with depth, but stress drop remaining constant; (b) attenuation decreasing with depth and stress drop increasing with depth (by a factor of 3 between the two populations); and (c) attenuation constant with depth (as assumed in previous spectral decomposition studies) and stress drop increasing with depth (again by a factor of 3). We calculate synthetic recorded spectra using Equation 2 which combines the simple, circular, Brune source model (Brune, 1970) with exponential attenuation (e.g., Anderson & Hough, 1984).

$$X(f) = \frac{M_0}{1 + \left(\frac{f}{f_c}\right)^2} e^{-\pi f t^*} \tag{2}$$

The synthetic spectrum (X) is calculated from the seismic moment (M_0) and corner frequency (f_c), over frequency (f). The attenuation $(t^*) = t/Q$ where t is the travel time, and Q is frequency independent for the purposes of clarity. We assume moment magnitude (M_W) of 3 and 2, for the large and small earthquakes,

10.1029/2021JB022314

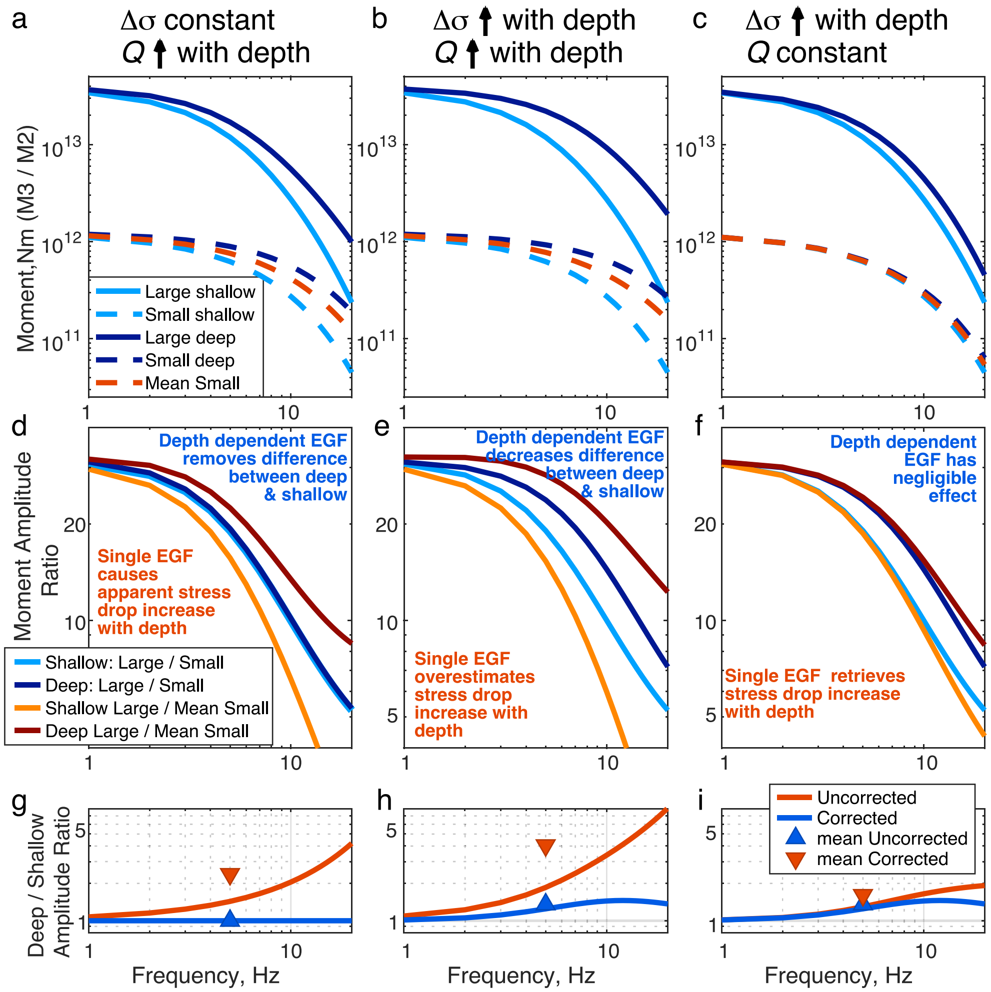

Figure 5. Effects of increasing Q and stress drop ($\Delta\sigma$) with depth on synthetic spectra in three example cases. Top row: Brune spectra of large (M3.5, solid lines), shallow (pale blue) and deep (dark blue) events and small (M2.5, dashed lines), shallow (pale blue) and deep (dark blue) events (red is mean of small shallow and deep) for (a) constant $\Delta\sigma$, Q increasing with depth, (b) Q and $\Delta\sigma$ increasing with depth, and (c) constant Q, $\Delta\sigma$ increasing with depth (parameters in Table 2). Middle row: spectral ratios of deep large to deep small (dark blue), shallow large to shallow small (pale blue), deep large to the mean of small (dark red) and shallow large to the mean of small (orange). (d) Constant $\Delta\sigma$, Q increasing with depth—difference between event ratios disappears when depth—dependent correction included, (e) Q and $\Delta\sigma$ increasing with depth—difference between event ratios decreases when depth-dependent correction included, and (f) constant Q, $\Delta\sigma$ increasing with depth—depth dependent correction has no effect. Bottom row: Comparison of spectral ratios with and without depth dependent correction, (g) ratio of uncorrected deep/shallow ratios (red: ratio of dark and pale red in (d) compared to similar ratio for corrected ratios (blue: ratio of dark and pale blue in (e). Triangles show the mean values over the representative frequency range 2–20 Hz. (h, i) The same comparison for the other two example cases.

respectively, and $t = 10$ s for all events in this simple example. We assume that the stations are sufficiently distant that ray paths leaving the events travel nearly horizontally, such that the shallow-event rays spend more time in the low-Q layers near the surface than the deeper events (see Figure 4). For the purposes of this synthetic exercise, we simplify and approximate the attenuation difference using fixed t^* values for the deep and shallow events. The assumed parameters are given in Table 2. Varying the assumed geometry and parameters of the model will obviously affect the shapes of the calculated spectra. The aim of our synthetic example is simply to demonstrate the pattern of the effects, and show that they can be significant.

In all cases in the top row of Figure 5, we observe that the deeper events have relatively more energy at high frequencies than do the shallow, consistent with the observations in Figures 2 and 3.

Table 2
Source Parameters Assumed to Calculate the Synthetic Spectra Shown in Figure 5

	f_c (Hz) M_W 3 (large)		f_c (Hz) M_W 2 (small)			
Case	Deep	Shallow	Deep	Shallow	t^*deep (s)	t^*Shallow (s)
a: Q increases with depth, $\Delta\sigma$ constant	5.6	5.6	17.8	17.8	0.0171	0.04
b: Q and $\Delta\sigma$ increase with depth	8.1	5.6	25.6	17.8	0.0171	0.04
c: Q constant, $\Delta\sigma$ increases with depth	8.1	5.6	25.6	17.8	0.04	0.04

Note. Values are calculated assuming the same travel time (10 s) for all events, and a corner frequency of 10 Hz for a shallow M_W2.5. These values are purely illustrative.

The middle row of Figure 5 demonstrates what we would expect to observe using our EGF-based approach for the different scenarios. Without any correction for depth dependent attenuation, there is a clear difference between the spectral ratios obtained for large deep and large shallow earthquakes in all cases (difference between the dark and light red curves, see legend). If attenuation varies with depth, then correcting for this by using depth-specific EGFs (dark and light blue curves) significantly decreases the difference between the deep and the shallow ratios; the blue curves are closer to one another than the red curves in Figures 5d and 5e. In the case of constant attenuation with depth (Figure 5f) but increasing stress drop, the difference between the two blue curves is little different from that between the two red ones; the small difference results from the varying corner frequency of the smaller EGF events because of the depth-dependent stress drop.

The bottom row of Figure 5 essentially shows the ratios of the deep to shallow earthquake spectra with (blue) and without (red) a correction for depth-dependent attenuation. These correspond to the ratio of the two blue ratios and the two red ratios shown in the middle row. The triangles of the same color indicate the mean value of the ratios in the frequency range 2–20 Hz, typical of the studies used in our analysis. When stress drop is constant, but Q increases with depth (Figure 5g) the blue ratio is close to one, systematically lower than the red ratio. When both stress drop and Q increase with depth (Figure 5h) then the blue ratio is larger than one, but systematically lower than the red ratio. When stress drop increases with depth, but Q is constant (Figure 5i) then there is no difference between the two ratios, except near and above the EGF corner frequency.

For clarity in this simple example, we implicitly assume that both the shear wave velocity and the rupture velocity are constant, independent of depth. If the rupture velocity increases with depth, perhaps as a constant function of shear wave (or even P wave) velocity, then this would cause a deeper earthquake to have a higher corner frequency than a shallower one, even if they both had the same stress drop. Hence, a constant stress drop with depth could look more like the middle, or even the righthand columns of Figure 5, depending on the rate of increase in rupture velocity with depth.

We use the EGF-based approach described above to investigate the event spectra from the different spectral decomposition studies. For each region, we stack the event spectra in different magnitude and depth bins (by calculating the mean of the log spectral amplitudes), calculate ratios between large and small events and compare the results to the middle and bottom rows of Figure 5. For simplicity, we first focus on the systematic variation in the ratios and corner frequencies. In the Discussion, we explicitly look at the effects of including varying rupture velocity. We use the consistent color scheme introduced in Figures 4 and 5 throughout the paper to improve clarity.

4.2. Application to Data

To investigate the causes of the varying spectral shape with source depth observed in the data (Figures 2 and 3) we stack the event spectra for all the earthquakes in magnitude and depth bins to obtain stable mean spectra that we can compare following the approach outlined in the synthetic test (Figure 5). We stack the data to focus on the systematic effects common to a population of events, rather than the variation between individual earthquakes.

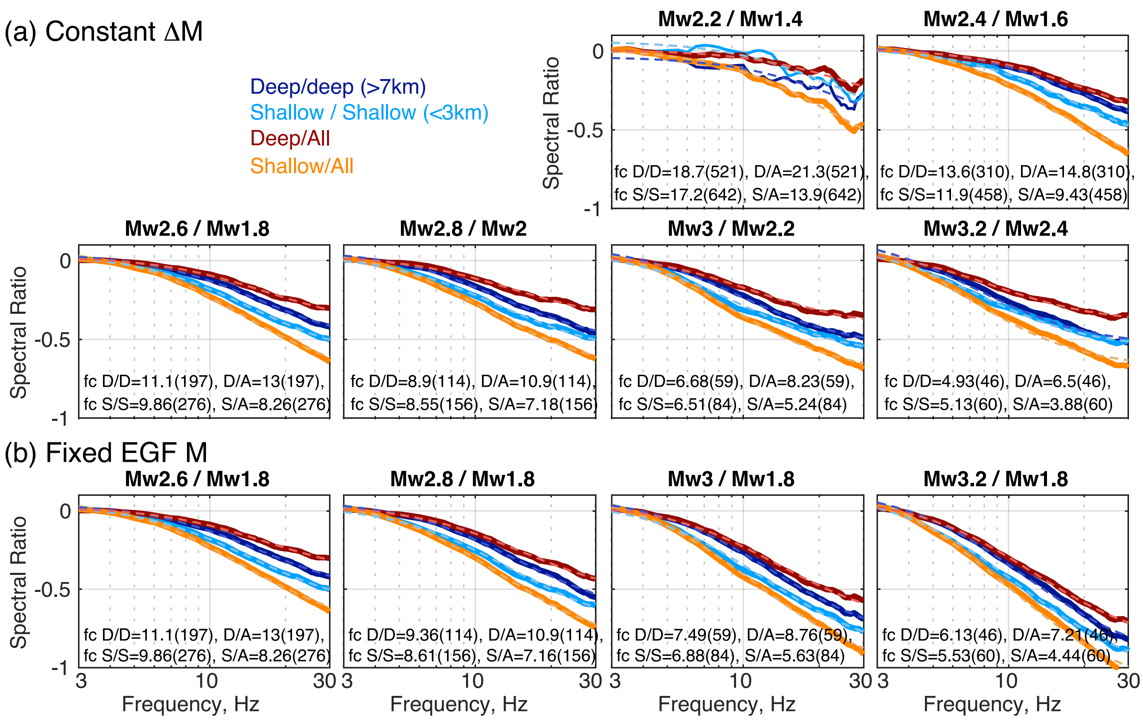

Figure 6. Spectral ratios of stacked large to small Ridgecrest aftershocks, to investigate the effects of a depth dependent EGF correction. Compare to the synthetic example in Figure 5. Each plot shows spectral ratios (solid lines) of the stacked large deep events to the stacked small deep events (dark blue), the large shallow events to the small shallow events (pale blue), the large deep events to all the small events (dark red) and the large shallow events to all the small events (orange). The title of each plot indicates the minimum Mw of the large and small events, both with a range of 0.2Mw. (a) For a constant Mw difference between large and small earthquakes, and (b) for a constant-sized Mw for the small earthquakes. The dashed lines are the fits of the Brune omega-squared spectral ratios to the average data ratios. The corner frequency of the best fitting ratio is given on each plot, with the number of larger events in the ratios in parentheses (D = deep, S = shallow, and A = all). Thinner lines indicate less than 10 large or small events were included in the mean ratios. The blue (depth-corrected) deep and shallow event spectral ratios are consistently closer together than the red ratios that assume no dependence of attenuation with depth (compare to Figures 5d and 5e).

For each study we select a shallow depth range and a deep depth range (Table 1). These depths are guided by the observed changes with depth of both the frequency content of the event spectra and the velocity structure (Figure 3), and the need for sufficient earthquakes in the two depth ranges for stable stacking. We perform our analysis comparing earthquakes from these two depth ranges, but to ensure that our results are not dependent on these selected values, we also repeat the entire analysis simply dividing each data set at its median value into a shallower and deeper event population. We do not try using the same depth ranges for different data sets because the different earthquake populations have very different depth distributions (Figure 3). Source spectral shape depends on earthquake magnitude and so we divide the earthquakes into bins of 0.2Mw units to enable the averaging of stacking.

For each dataset, we stack the event spectra in each magnitude and depth bin by calculating the geometric mean spectrum for each bin. We then calculate the ratios between pairs of large and small (EGF) events as described in the synthetic example. For the ratios without any depth correction, we include earthquakes from the entire depth range of the study (not just the deep and shallow ranges) in the stack of small EGF events. We try all available magnitude bins, but only use those with at least five large and five small events. The results for the Ridgecrest aftershock sequence are shown in Figure 6, and the results of other example data sets are shown in the Supporting Information S1 (Figure S4). We select the magnitude bin for the EGF events in two different ways. First, we use a constant magnitude difference (0.8 Mw units) between the large and small events (top two rows of Figure 6). Second, we select one fixed Mw bin as the preferred EGF and apply it to all Mw bins at least 0.8 Mw units larger (bottom row in Figure 6). One magnitude pairing is therefore included in both (Mw2.6/Mw1.8 in Figure 6). We apply the two approaches to ensure that our results are not dependent on the method of selecting the EGF, and they are also useful as a check on the uncertainties in our analysis. Clearly if earthquakes of different depth, in any Mw bin, have different stress drops, then this will be true regardless of the exact magnitude of the EGF events.

Each panel of Figure 6 can be compared directly to Figures 5d–5f, to distinguish between depth-dependent source and path effects. In all panels of Figure 6, the difference between the source spectral ratios for deep and shallow events decrease when depth-specific EGF corrections are applied. In some cases, the deep and shallow spectral ratios become almost indistinguishable (e.g., Mw3.2/Mw2.4) when using depth-specific EGFs, resembling Figure 5d in which all the depth dependence is a consequence of attenuation. Most panels of Figure 6 more closely resemble Figure 5e, exhibiting a significant decrease in depth dependence when using depth-specific EGFs.

We then fit the spectral ratios (as shown in Figure 6) using the Brune source model:

$$\frac{X_1(f)}{X_2(f)} = \frac{e_1(f)}{e_2(f)} = \frac{M_{0^1}}{M_{0^2}} \frac{\left[1+\left(\frac{f}{f_{c^2}}\right)^2\right]}{\left[1+\left(\frac{f}{f_{c^1}}\right)^2\right]} \tag{3}$$

which has been shown to work well for stacked spectra (e.g., Shearer et al., 2006, 2019); subscripts 1 and 2 refer to the larger event stack and the smaller event stack, respectively. Many of the datasets we consider are unlikely to have sufficient resolution to separate completely the path and source effects (e.g., Shearer et al., 2019), and so we fix the corner frequency of the stacked EGF events (denominator) in the spectral ratios (f_{c^2}). We first assume a stress drop of 3 MPa (e.g., Abercrombie, 1995; Shearer et al., 2006) for the smaller stacked events, and calculate the corner frequency following Madariaga (1976) and Eshelby (1957)

$$f_{c^2} = k\beta\left(\frac{16\Delta\sigma}{7M_{0^2}}\right)^{1/3} \tag{4}$$

assuming $k = 0.32$ and an average shear wave velocity, $\beta = 3{,}500$ m/s, for all depth bins and data sets. These fits are shown in Figure 6, and for other example data sets in the Supporting Information S1 (Figure S4). We then try different values to investigate their effects on our results, as discussed in the next section. We do not expect our analysis to obtain the actual stress drops of the various event stacks; rather, we use the spectral ratio modeling simply to quantify the systematic patterns that can distinguish between depth dependent source and path effects.

5. Results and Discussion

The aim of our analysis is to distinguish between depth dependent source and path effects within the event spectra obtained by spectral decomposition, which in turn is based on a simplified approximation of path-dependent attenuation. Our results are also relevant to any EGF-based analysis, whether in the frequency or time domain, indicating that depth should be included as a constraint in the selection of EGF events (e.g., Abercrombie, 2015). Our approach involves comparing stacks of deep and shallow earthquake event spectra, divided by smaller stacked EGF earthquakes selected either from the same depth ranges (depth-specific EGFs to correct for depth-dependent path effects) or averaged over the entire depth range (no correction for depth-dependent path effects). Figure 6 shows how using depth-specific EGFs systematically decreases the differences between the shallow and deep source spectra. Figures 7–9 show the results for the datasets with the most earthquakes (see Table 1 for numbers) which are most robust, and also for the Hayward fault analysis by Hardebeck and Aron (2009) that found a strong increase in stress drop with depth. Following the color scheme in Figures 4 and 5, blue symbols represent measurements made with a correction for depth-dependent path effects (i.e., depth-specific EGFs) and red symbols represent measurements without a correction for depth-dependent path effects. The results from all the datasets are shown in the Supporting Information S1 (Figures S5–S8).

Figure 7 compares the ratios of the deep and shallow, stacked, EGF-corrected, event spectra for different magnitude bins, and can be understood by direct comparison with Figures 5g–5i. In most regions the red

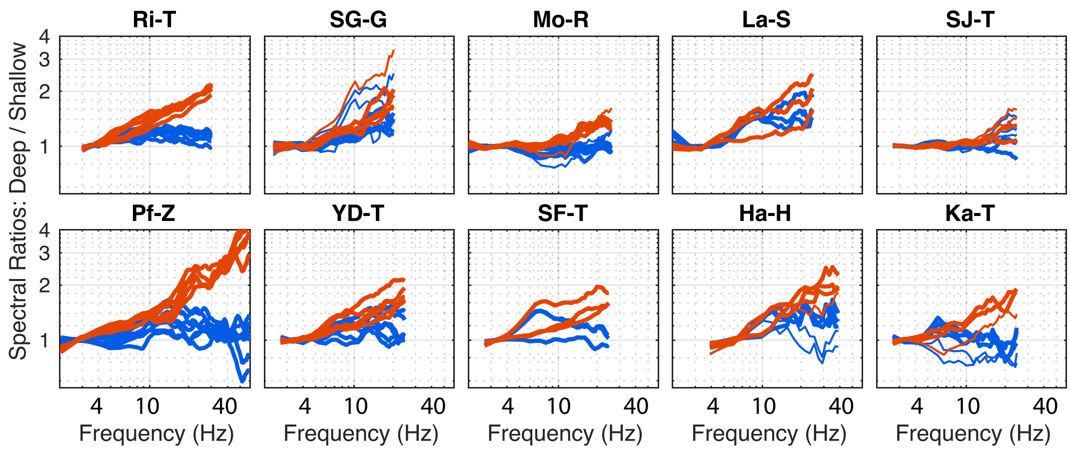

Figure 7. Depth differences in the event spectra: ratios of ratios—compare to Figures 5g–5i). Uncorrected for Depth (red): The large deep and shallow events are divided by the same selection of small events, and so the difference between the deep and shallow ratios is simply the ratio of the mean deep large event spectra to the mean shallow (each ratio is the mean for a different large Mw bin). Corrected for Depth (blue): In this case, for each large Mw bin, the blue curve represents the ratio of the (mean large deep spectra divided by the small deep spectra) to the (mean large shallow spectra divided by the small shallow spectra); again each ratio is for a large Mw bin. The similarity of the slope of the red curves in each region demonstrates that the difference in frequency content between shallow and deep events is independent of magnitude. The smaller slope of the blue curves shows that using the correct depth small EGF events can remove this depth-dependence to the frequency content, suggesting it is largely an attenuation effect.

ratios (deep, EGF corrected/shallow, EGF corrected, where EGFs are independent of source depth) increase with frequency, suggesting the deeper earthquakes may contain more higher frequency energy than similar sized shallow events, but this difference is systematically reduced by the use of depth-specific EGF events (blue curves: deep, EGF corrected/shallow, EGF corrected, where EGFs are depth specific). This effect is strongest in the Ridgecrest and Parkfield datasets. Comparison of Figure 7 with the synthetic examples in

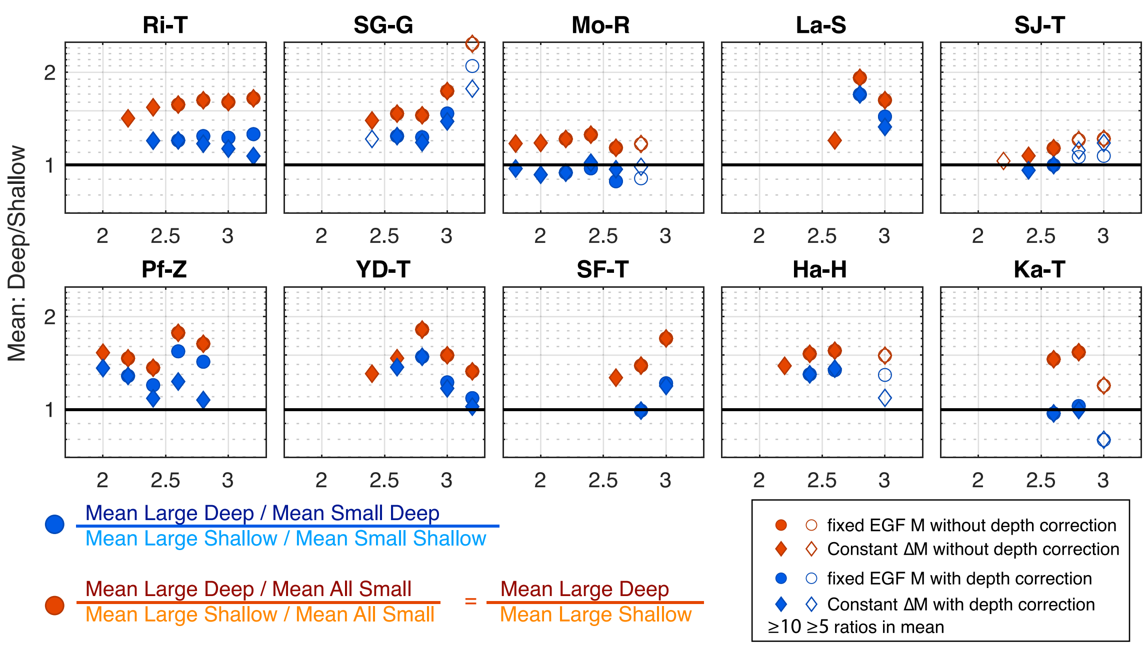

Figure 8. Comparison of mean amplitude ratios of deep/shallow for each region—compare to Figures 5g–5i. The symbols indicate the mean values of the red and blue ratios shown in Figure 7, in the frequency range 2–20 Hz. Solid symbols represent ratios with at least 10 ratios, and open symbols those with at least five; diamonds are for a constant different in magnitude between large and small, and circles are for a constant sized small event range. Note that the depth correction is able to remove much, and in some cases all, of the difference between the deep and shallow spectra. The interpoint variation between diamonds and circles, and between different magnitudes is indicative of the uncertainties.

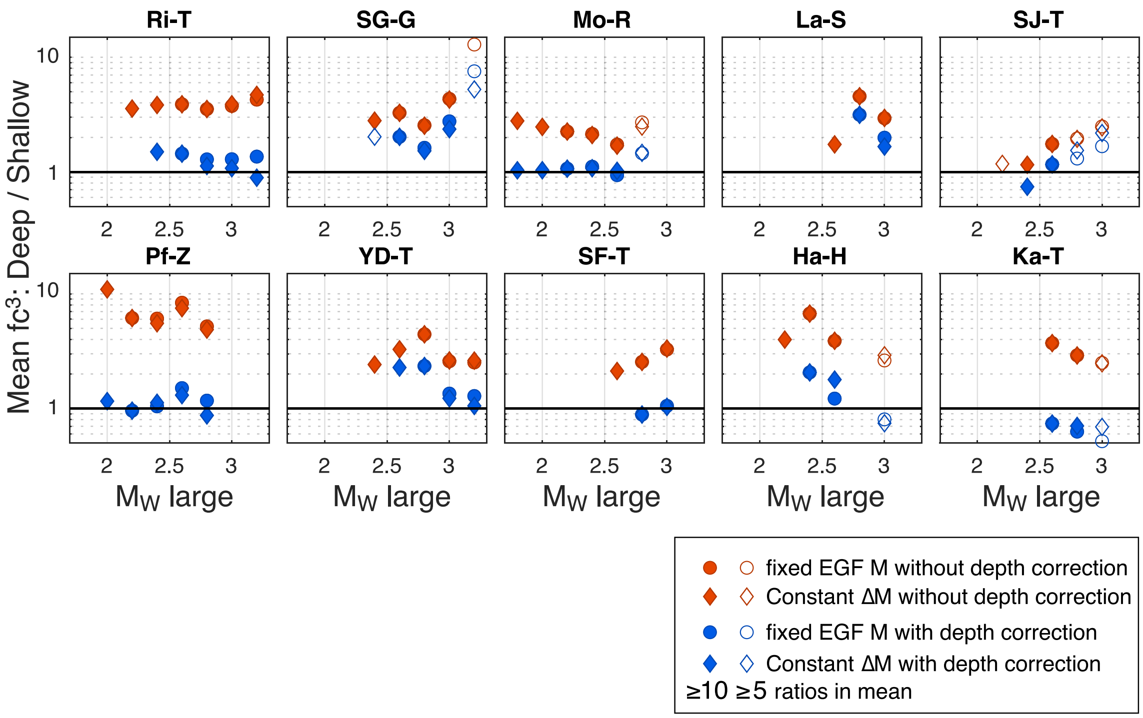

Figure 9. Spectral ratio modeling results with and without correction for depth-dependent attenuation. The ratios of the calculated stress drop (proportional to corner frequency cubed, fc^3) of the deep to the shallow earthquakes are shown for each data set, with (blue) and without (red) a correction for depth-dependent attenuation, plotted against the minimum magnitude of the large earthquakes. For example, the Ridgecrest plot shows the ratios of the cubed corner frequencies for the different model fits in Figure 6. Solid symbols represent ratios with at least 10 ratios, and open symbols those with at least five; diamonds are for a constant different in magnitude between large and small, and circles are for a constant sized small event range. For most data sets, the depth corrections decrease the apparent difference in stress drop between the deep and small events, independent of the magnitude of the large or small events included.

Figure 5, shows most similarity with panels 5d and 5e; this implies that using EGFs from the correct depth range can remove a significant amount of the apparent difference between deep and shallow earthquake sources.

To quantify the effect of the different EGF corrections, we calculate the mean values of each of the blue and red (with and without including depth-specific EGF corrections) ratios (Figures 8 and S6) in the frequency range 2–20 Hz. These results can be directly compared to the synthetic models in Figures 5g–5i. In each study, the amplitudes of the ratios without including an EGF correction for source depth (red symbols) are systematically higher than those that do use depth-specific EGFs (blue symbols); the effect is weaker in datasets that exhibit little depth-dependence of any kind. There is no obvious reason why any real increase in either source properties or Q with depth would depend on either the magnitude of the larger events, or the magnitude of the EGF events. Any variation between the different symbols of the same color is more likely to represent uncertainties and variability from small populations of earthquakes, and the simplifying assumptions used in the stacking. We interpret the observation that the blue symbols using depth-specific EGFs are systematically closer to one in all cases, to indicate that much of the apparent difference in deep and small earthquakes observed in event spectra is an artifact of not including depth-dependent attenuation in the inversion.

The spectral ratio fitting confirms this result. Figures 9 and S7 show that after correction with the depth-specific EGF events, any increase in corner-frequency with depth becomes systematically smaller, and almost negligible. Again, the variability of symbols of a given color indicates the uncertainties in the measurements.

5.1. Effect of Depth Range Selection

These results are all based on selecting representative depth ranges for the shallow and deep earthquake populations. Although these selections are based on the velocity structures and the earthquake depth distributions, they are somewhat arbitrary and subjective. To ensure that they are not strongly influencing the results, we repeat the entire analysis, but instead of selecting the depth ranges, we simply divide each of the earthquake populations in half at their respective median depths. As shown in Figure S8a, there is a small reduction in the effects of using the correction for depth-specific EGFs, compared to Figure 9. This is expected as the two populations compared in Figure S8a include more intermediate depth events and are less distinct. The general observation of decreasing difference (between shallow and deep earthquakes) following application of depth-specific EGFs remains clear and consistent across the entire dataset indicating that our precise choices of depth are not affecting our main conclusion.

5.2. Effect of Spectral Fitting Assumptions

The comparisons using spectral fitting are consistent with the basic spectral observations in Figures 7 and 8, but do involve assumptions and constraints that may affect the results. One significant assumption is the value to which we fix the corner frequency of the EGF events (f_{c2}) in the ratios. The limited bandwidth of most of the data means that f_{c2} is very unlikely to be resolvable as a free parameter (e.g., Abercrombie, 2015; Ruhl et al., 2017; Shearer et al., 2019); the majority of fixed and inverted f_{c2} values are between 10 and 40 Hz. In our analysis, we assume that f_{c2} is independent of the depth of the EGF earthquakes, and it is possible that this assumption of depth independence may affect our modeling of the depth-dependence of the larger earthquakes. We therefore perform a series of inversions to investigate the constraints and tests to determine whether our results could be significantly biased by our assumptions.

First, we consider using a mean stress drop that is three times higher to calculate all values of f_{c2}, regardless of depth. This results in an almost identical variation with depth to that found with 3 MPa and shown in Figure 9. This forced higher stress drop for the smaller earthquakes resulted in consistently higher corner frequencies and stress drops for the larger earthquakes, but also significantly higher misfit variance in almost all datasets (Figure S9).

Second, we try fixing the stress drop of the deep earthquakes used to calculate f_{c2} to be a factor of 2, three or 5 higher than that assumed for the shallower groups of earthquakes. (This test also addresses the effects of an increasing velocity with depth causing an increasing f_{c2} with depth even if stress drop is constant.) This resulted in the depth-specific EGF correction removing less of the depth dependence to the stress drop for the larger earthquakes (e.g., Figure S8b). Comparison of the misfit variances from these tests (Figure S9) shows that, on average, the observed spectral ratios in all datasets are consistently fit better with a constant stress drop for the smaller EGF earthquakes, independent of depth, than with the depth-dependent assumption. This is consistent with the visual comparison of the observed event spectral ratios in Figures 6 and 7.

Finally, we also try allowing f_{c2} as a free variable in the spectral ratio fitting, but, as expected, find the results to be unconstrained. We conclude this using the same approach as Shearer et al. (2019). Stacked event spectra of the same smaller earthquakes, from all depths, are used as EGFs for both deep and shallow earthquakes, when the effects of a depth correction are ignored. We obtain systematically different values for f_{c2} for the same event stack when it is used as the denominator for deep and shallow larger events. We do not know which value of f_{c2} is correct, but we do know that the same set of earthquakes should have the same absolute value, independent of the events to which it is compared. Therefore, the different values obtained indicate the lack of constraint in the spectral fitting, and so we limit our interpretations to the results of fitting with fixed values of f_{c2}.

5.3. Relationship Between Attenuation and Velocity Structure

In Figure 3, we compare the variation with depth of the average spectral shape of earthquakes in each region with the local P-wave velocity structure. Although the S wave velocity is used in Equation 4, all the spectra used in this analysis are calculated from P waves. Event spectra that extend over a wider range of source-region velocity appear to show higher variation in frequency content. Since both attenuation and velocity are related to material properties of the structure, then some relation between them is expected. For example, Brocher (2008) and Eberhart-Phillips et al. (2014) showed that Q increases with velocity but there is considerable scatter and no simple relationship.

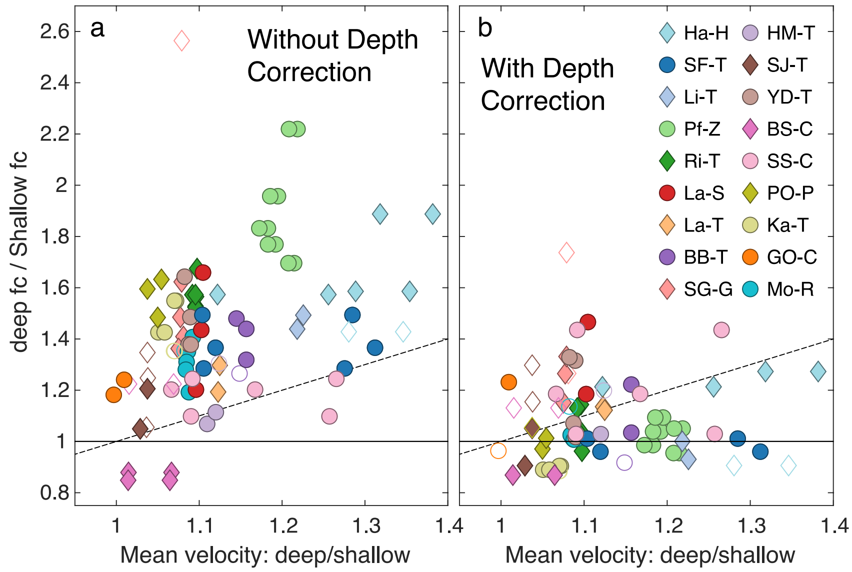

Figure 10. Comparison of relative source parameters with difference in P-wave velocity. The ratios of corner frequencies between the deep and shallow earthquakes calculated using the approaches shown in Figures 9 and S7 are plotted against the ratio of the average P-wave velocity at the depths of the respective deep and shallow event populations included. Color is by data set, with alternating symbols to ease distinction. Multiple symbols per data set represent the different magnitude bins, and also the use of the alternative velocity models. (a) Without correction for depth dependent attenuation and (b) with correction for depth dependent attenuation. The black dashed line represents a constant stress drop with depth, if rupture velocity is proportional to P-wave velocity.

In Figure 10, we compare the corner frequencies of deep and shallow earthquakes of the same magnitude, calculated assuming fixed, depth-independent, f_{c2}, to the source region velocity. We calculate the mean velocity in the depth range of the events in each population used in the spectral ratios, using the structures in Tables 1 and S1–S10. We then plot the ratio of the deep and shallow source parameters against the ratio of the deep to shallow source velocity for each spectral ratio. All points from regions with two alternative velocity models (for example, both sides of the Hayward fault) are plotted twice. Figure 10a shows the relationship without using the depth-specific EGFs; there is a large scatter, but a general increase in apparent corner frequency difference with increasing velocity difference can be seen. This increase is larger than could be explained by a constant stress drop, even allowing the rupture velocity to increase proportional to the P wave velocity (Equation 4, dashed line in figure). Figure 10b shows the same results after the spectral ratios are corrected using the depth-specific EGFs. The differences with depth are smaller, and no longer show any obvious dependence on source depth. Most of the variability is within the range that could be explained by increasing rupture velocity with depth. This comparison suggests that although the velocity structure is inadequate for a real estimate of attenuation, variation in velocity with depth could be used as a first order indication of the depth-dependence of the attenuation (e.g., Eberhart-Phillips et al., 2014). Also, if the difference in velocity with depth is known, then Figure 10 provides a guide to the size of the effect depth-dependent attenuation could have on estimates of corner frequency.

5.4. Implications for Depth Dependence of Earthquake Stress Drop

Our analysis has shown that the increase in Q with depth can exert a first order effect on recorded seismograms, that cannot be ignored when investigating changes in stress drop with depth. This result is in good agreement with the earlier studies of Edwards et al. (2008) and Edwards and Rietbrock (2009) who demonstrated the effects of including depth dependent attenuation on stress drop measurements. Our analysis implies that much, if not all, the increase in stress drop with depth reported by previous spectral decomposition studies could be an artifact caused by inadequate consideration of depth-dependent attenuation.

As pressure, and hence normal stress, increases with depth in the earth, it seems reasonable that the stress release in earthquakes should increase also (e.g., Scuderi et al., 2016; Sibson, 1974). Otherwise, the differential stresses involved in faulting must somehow remain constant, despite the increasing pressure, or the deeper earthquakes must release a smaller fraction of the peak differential stress. Whether we can resolve real increase in stress drop with depth from existing earthquake recordings remains open to question. Like previous work, our results are also subject to uncertainties, and depend on assumptions about the corner frequency of the smallest earthquakes, and so some increase in stress drop with depth is well-within the constraints. In the future, further work is required at the interface of attenuation tomography and source modeling to investigate the real resolution of both, and to balance the need to account for spatially (and temporally) varying attenuation, and different source geometries, without increasing the number of free parameters well beyond the constraints of the available data.

To investigate resolution, and spatial variability, Pennington et al. (2021) performed a detailed comparison of multiple methods of calculating stress drop. To address the possibility of depth dependent attenuation in spectral decomposition approaches, they calculated different empirical correction spectra for the earthquakes in the basement to those in the overlying sediments. This significantly decreased the depth dependence of the resulting stress drop estimates. They found best agreement between the various studies in the central depth range of the events, within the upper kilometers of the basement. Zhang et al. (2019) investigated the effects of using separate empirical correction spectra for earthquakes in different depth ranges in their spectral decomposition analysis of borehole-recorded earthquakes at Parkfield. They too found that after including changes in Q with depth, only negligible change in stress drop with depth remained. Ruhl and Abercrombie (2020) implemented a similar approach for the Mogul earthquakes, and obtained similar results that are consistent with the detailed, smaller scale EGF analysis by Ruhl et al. (2017) which found no significant depth dependence to stress drop. These studies are a first step toward improving resolution of the trade-off between source and path in spectral decomposition analyses, without simply adding so many free parameters as to make the whole problem completely unconstrained. Using depth-dependent correction functions to account for changes in Q with depth is not fully satisfactory, however, as it comes after the initial spectral decomposition in which the path terms are assumed to be independent of source depth, and only depend on travel time.

Similar to the original empirically-corrected spectral decomposition analyses, the results of the generalized inversion studies such as Bindi, Spallarossa, et al. (2020) and Oth et al. (2011) do not explicitly consider an increase in Q with source depth. They too should be considered potentially biased in the same manner as the spectral decomposition analyses. For example, at Ridgecrest Bindi, Zaccarelli, et al. (2020) obtained a similar apparent depth dependence to stress drop as Trugman (2020) and also did not explicitly consider an increase in Q with source depth. Bindi et al. (2021) performed a subsequent study and identified a combination of depth and distance varying attenuation and stress drop increasing with depth that were able to fit the observed spectra. Given the large trade-offs among the parameters this is not surprising, and they did not investigate the uniqueness of their solution. Bindi, Spallarossa, et al. (2020) and Bindi et al. (2021) also used variable time windows, each incorporating different combinations of P, S and coda energy, which makes it hard to compare their results directly with the short P-wave windows used in the present analysis. Parker et al. (2020) investigated the performance of ground motion prediction equations on the aftershocks of the 2019 Ridgecrest earthquake and observed that the deeper earthquakes exhibited higher ground acceleration, consistent with their having higher stress drop. Like the studies by Trugman (2020) and Bindi, Zaccarelli, et al. (2020) of the same sequence, they did not include any dependence of attenuation on source depth in their analysis. In empirical ground motion prediction, it is not essential to distinguish whether source or path effects cause a trend when interpolating within a data set, but it is required to extrapolate predictions to different regions, or larger magnitude earthquakes (e.g., Bommer et al., 2007).

The results of EGF studies in which a collocated small earthquake is used to compensate for all the path and site effects should, theoretically, be unaffected by the tradeoffs between attenuation and source. In practice, however, the lack of suitable EGF events, and uncertainties in their locations (especially depth) mean that often an EGF may not fully compensate for the attenuation. Abercrombie (2015) and Kane et al. (2013) showed how EGF selection can affect stress drop measurements; clearly if the EGF is imperfect, then not only will the source spectral shape be biased, but the duration of the source time function will also be affected, and so time-domain measurements are not immune to this trade-off. Huang et al. (2017) and Boyd et al. (2017) both used spectral ratio approaches to investigate stress drop dependence on depth and tectonic setting, but had insufficient earthquakes to only use EGFs of similar depth to the main events. Boyd et al. (2017) included the effects of increasing velocity and rigidity with depth on the estimates of seismic moment, rupture velocity and hence stress drop, finding that stress drop increased with depth. However, in their cluster-based analysis, they combined earthquakes from a similar range of depths and velocities as the analyses revisited here, making no correction for the different source depths. It is possible, therefore, that the increase in stress drop with depth that they reported is an artifact, or over-estimate. Unlike the other studies discussed, Boyd et al. (2017) used coda wave spectra in their analysis. Mayeda et al. (2007) showed that coda wave measurements are more stable, and less sensitive to spatial separation between main and EGF events than direct wave measurements, but they did not specifically consider separation in source depth. Coda wave generation is observed to vary with depth, especially in the shallow layers of the crust (e.g., Voyles et al., 2019). Walter et al. (2017) included source depth in their selection of earthquakes for coda wave spectral ratio analysis in Oklahoma. They observed an increase in stress drop with depth too large to be easily explained as an artifact of attenuation or velocity structure, but for only a relatively small number of events. Trugman and Savvaidis (2021) observed no clear depth-dependence in stress drop for seismicity in the Pecos area of west Texas, though the large depth uncertainties of earthquakes recorded in this region at present renders this finding unsurprising.

6. Conclusions

We investigate whether the increases in stress drop with depth reported by spectral decomposition earthquake studies are real, or potentially an artifact of neglecting to correct sufficiently for depth variation in attenuation (Q). We combine the event spectra calculated for over 50,000 earthquakes (M0-5) from 12 studies in California, Nevada, Kansas, and Oklahoma. We analyze spectral ratios between large and small events as a function of source depth, to explore the relative importance of source and attenuation contributions to the observed depth dependence in high-frequency radiation and corner frequency.

We find that correcting the earthquake event spectra with depth-specific EGFs can remove most, if not all, of the apparent stress drop increase with depth previously observed in the original studies. The largest corrections are observed in regions with the largest velocity increase with depth. We conclude that source spectral analyses, whether using spectral decomposition, EGFs, or any other approach, should not assume path terms are independent of source depth. More explicit depth-dependent attenuation models or depth-specific empirical corrections are required to resolve real variation of earthquake source processes with depth in the earth.

Data Availability Statement

This study uses the event spectra calculated in the published studies listed in Table 1, and cited in the References. The original waveforms are available from the Southern California Earthquake Data Center (SCEDC (2013): Southern California Earthquake Center (SCEC), Caltech, Dataset, https://doi.org/10.7909/C3WD3xH1. The SCEDC and Southern California Seismic Network (SCSN) are funded through U.S. Geological Survey Grant G20AP00037, and SCEC), the Northern California Earthquake Data Center (NCEDC), https://doi.org/10.7932/NCEDC, including the High Resolution Seismic Network (HRSN) https://doi.org/10.7932/HRSN, operated by the UC Berkeley Seismological Laboratory, and the Nevada Seismic Network (https://doi.org/10.7914/SN/NN). The other waveforms are available from IRIS, as follows: https://doi.org/10.7914/SN/GS; UC San Diego (2013). *Central and Eastern US Network*. International Federation of Digital Seismograph Networks (IFDSN). https://doi.org/10.7914/SN/N4; USGS Earthquake Science Center (2009). *NetQuakes*. IFDSN. https://doi.org/10.7914/SN/NQ; Darold (2014) 4D Integrated Study Using Geology, Geophysics, Reservoir Modeling & Rock Mechanics to Develop Assessment Models for Potential In, IFDSN. https://doi.org/10.7914/SN/ZD_2014; Oklahoma Geological Survey, 1978. Oklahoma Seismic Network, IFDSN, https://doi.org/10.7914/SN/OK; Nanometrics Seismological Instruments, 2013. Nanometrics Research Network, IFDSN, https://doi-org/10.7914/SN/NX. The velocity structures used are cited in Table 1, and included in the Supporting Information S1.

Acknowledgments
We are grateful to Malcolm White and Evan Hirakawa for extracting the representative 1D velocity models in the relevant regions of southern and northern California, respectively. Discussions with Donna Eberhart-Phillips and Annemarie Baltay, and reviews by Yihe Huang (Associate Editor), Oliver Boyd and two anonymous reviewers greatly improved the manuscript. This work was supported by funding from SCEC (Awards 19163 and 20097). SCEC is funded by NSF Cooperative Agreement EAR-1033462 and USGS Cooperative Agreement G12AC20038. This is SCEC publication number 11037.

References

Aagaard, B. T., Graymer, R. W., Thurber, C. H., Rodgers, A. J., Taira, T., Catchings, R. D., et al. (2020). *Science plan for improving three-dimensional seismic velocity models in the San Francisco Bay region, 2019–24* (37 p.). U.S. Geological Survey Open-File Report 2020–1019. https://doi.org/10.3133/ofr20201019

Abercrombie, R. E. (1995). Earthquake source scaling relationships from -1 to 5 *ML*, using seismograms recorded at 2.5 km depth. *Journal of Geophysical Research*, *100*, 24015–24036. https://doi.org/10.1029/95jb02397

Abercrombie, R. E. (1997). Near surface attenuation and site effects from comparison of surface and deep borehole recordings. *Bulletin of the Seismological Society of America*, *87*, 731–744.

Abercrombie, R. E. (2015). Investigating uncertainties in empirical Green's function analysis earthquake source parameters. *Journal of Geophysical Research: Solid Earth*, *120*, 4263–4277. https://doi.org/10.1002/2015JB011984

Abercrombie, R. E. (2021). Resolution and uncertainties in estimates of earthquake stress drop and energy release, *Philosophical Transactions of the Royal Society A*, *379*, 20200131. https://doi.org/10.1098/rsta.2020.0131

Abercrombie, R. E., Bannister, S., Ristau, J., & Doser, D. (2017). Variability of earthquake stress drop in a subduction setting, the Hikurangi Margin, New Zealand. *Geophysical Journal International*, *208*, 306–320. https://doi.org/10.1093/gji/ggw393

Allmann, B. P., & Shearer, P. M. (2007). Spatial and temporal stress drop variations in small earthquakes near Parkfield, California. *Journal of Geophysical Research*, *112*, B04305. https://doi.org/10.1029/2006JB004395

Anderson, J. G., & Hough, S. E. (1984). A model for the shape of the Fourier amplitude spectrum of acceleration at high frequencies. *Bulletin of the Seismological Society of America*, *74*, 1969–1993. https://doi.org/10.1785/bssa0740062685

Bindi, D., Hoby, N. T., Razafindrakoto, M. P., & Oth, A. (2021). Stress drop derived from spectral analysis considering the hypocentral depth in the attenuation model: Application to the Ridgecrest Region, California. *Bulletin of the Seismological Society of America*. https://doi.org/10.1785/0120210039

Bindi, D., Spallarossa, D., Picozzi, M., & Morasca, P. (2020). Reliability of source parameters for small events in central Italy: Insights from spectral decomposition analysis applied to both synthetic and real data. *Bulletin of the Seismological Society of America*, *110*, 3139–3157. https://doi.org/10.1785/0120200126

Bindi, D., Zaccarelli, R., & Kotha, S. R. (2020). Local and moment magnitude analysis in the Ridgecrest Region, California: Impact on interevent ground-motion variability. *Bulletin of the Seismological Society of America*, *111*, 339–355. https://doi.org/10.1785/0120200227

Bommer, J. M., Stafford, P. J., Alarcón, J. E., & Akkar, S. (2007). The influence of magnitude range on empirical ground-motion prediction. *Bulletin of the Seismological Society of America*, *97*(6), 2152–2170. https://doi.org/10.1785/0120070081

Boyd, O. S., McNamara, D. E., Hartzell, S., & Choy, G. (2017). Influence of lithostatic stress on earthquake stress drops in North America. *Bulletin of the Seismological Society of America*, *107*(2), 856–868. https://doi.org/10.1785/0120160219

Brocher, T. M. (2008). Key elements of regional seismic velocity models for long period ground motion simulations. *Journal of Seismology*, *12*, 217–221. https://doi.org/10.1007/s10950-007-9061-3

Brune, J. (1970). Tectonic stress and the spectra of seismic shear waves from earthquakes. *Journal of Geophysical Research*, *75*, 4997–5009. https://doi.org/10.1029/jb075i026p04997

Byerlee, J. D., & Brace, W. F. (1968). Stick slip, stable sliding, and earthquakes-effect of rock type, pressure, strain rate, and stiffness. *Journal of Geophysical Research*, *73*(18), 6031–6037. https://doi.org/10.1029/jb073i018p06031

Chen, C. (2016). *Comprehensive analysis of Oklahoma earthquakes: From earthquake monitoring to 3D tomography and relocation (PhD dissertation)*. University of Oklahoma.

Chen, X., & Abercrombie, R. E. (2020). Improved approach for stress drop estimation and its application to an induced earthquake sequence in Oklahoma. *Geophysical Journal International*, *223*(1), 233–253. https://doi.org/10.1093/gji/ggaa316

Chen, X., & Shearer, P. M. (2011). Comprehensive analysis of earthquake source spectra and swarms in the Salton Trough, California. *Journal of Geophysical Research*, *116*, B09309. https://doi.org/10.1029/2011JB008263

Darold. (2014). *4D integrated study using geology, geophysics, reservoir modeling & rock mechanics to develop assessment models for potential in*. IFDSN. https://doi.org/10.7914/SN/ZD_2014

Dieterich, J. H. (1979). Modeling of rock friction: 1. Experimental results and constitutive equations. *Journal of Geophysical Research*, *84*(9), 2161–2168. https://doi.org/10.1007/BF00876539

Eberhart-Phillips, D. (2016). Northern California seismic attenuation: 3D *QP* and *QS* models. *Bulletin of the Seismological Society of America*, *106*, 2558–2573. https://doi.org/10.1785/0120160060

Eberhart-Phillips, D., Thurber, C., & Fletcher, J. B. (2014). Imaging P and S attenuation in the Sacramento–San Joaquin delta region, northern California. *Bulletin of the Seismological Society of America*, *104*(5), 2322–2336. https://doi.org/10.1785/0120130336

Edwards, B., & Rietbrock, A. (2009). A comparative study on attenuation & source-scaling relations in the Kanto, Tokai, & Chubu Regions of Japan, using data from Hi-Net & Kik-Net. *Bulletin of the Seismological Society of America*, *99*, 2435–2460. https://doi.org/10.1785/0120080292

Edwards, B., Rietbrock, A., Bommer, J. J., & Baptie, B. (2008). The acquisition of source, path and site effects from micro-earthquake recordings using *Q* tomography: Application to the UK. *Bulletin of the Seismological Society of America*, *98*, 1915–1935. https://doi.org/10.1785/0120070127

Eshelby, J. D. (1957). The determination of the elastic field of an ellipsoidal inclusion and related problems. *Proceedings of the Royal Society of London*, *241*, 376–396. https://doi.org/10.1098/rspa.1957.0133

Goebel, T. H. W., Hauksson, E., Shearer, P. M., & Ampuero, J. P. (2015). Stress-drop heterogeneity within tectonically complex regions: A case study of San Gorgonio Pass, southern California. *Geophysical Journal International*, *202*, 514–528. https://doi.org/10.1093/gji/ggv160

Goertz-Allmann, B. P., & Edwards, B. (2014). Constraints on crustal attenuation and three-dimensional spatial distribution of stress drop in Switzerland. *Geophysical Journal International*, *196*, 493–509. https://doi.org/10.1093/gji/ggt384

Hardebeck, J. L., & Aron, A. (2009). Earthquake stress drops and inferred fault strength on the Hayward fault, East San Francisco Bay, California. *Bulletin of the Seismological Society of America*, *99*, 1801–1814. https://doi.org/10.1785/0120080242

Hauksson, E., & Shearer, P. M. (2006). Attenuation models (Q_P and Q_S) in three dimensions of the southern California crust: Inferred fluid saturation at seismogenic depths. *Journal of Geophysical Research: Solid Earth*, *111*, B05302. https://doi.org/10.1029/2005JB003947

Hough, S. E., & Anderson, J. G. (1988). High-frequency spectra observed at Anza, California: Implications for Q structure. *Bulletin of the Seismological Society of America*, *78*, 692–707. https://doi.org/10.1785/bssa0780020692

Huang, Y., Ellsworth, W. L., & Beroza, G. C. (2017). Stress drops of induced and tectonic earthquakes in the central United States are indistinguishable. *Science Advances*, *3*, e1700772. https://doi.org/10.1126/sciadv.1700772

Kane, D. L., Kilb, D. L., & Vernon, F. L. (2013). Selecting empirical Green's functions in regions of fault complexity: A study of data from the San Jacinto Fault Zone, Southern California, *Bulletin of the Seismological Society of America 103*(2A), 641–650. https://doi.org/10.1785/0120120189

Kaneko, Y., & Shearer, P. M. (2015). Variability of seismic source spectra, estimated stress drop, and radiated energy, derived from cohesive-zone models of symmetrical and asymmetrical circular and elliptical ruptures. *Journal of Geophysical Research: Solid Earth*, *120*, 1053–1079. https://doi.org/10.1002/2014JB011642

Lomax, A. (2020). Absolute location of 2019 Ridgecrest seismicity reveals a shallow Mw 7.1 hypocenter, migrating and pulsing Mw 7.1 foreshocks, and duplex Mw 6.4 ruptures. *Bulletin of the Seismological Society of America*, *110*(4), 1845–1858. https://doi.org/10.1785/0120200006

Madariaga, R. (1976). Dynamics of an expanding circular crack. *Bulletin of the Seismological Society of America*, *66*, 639–666.

Marone, C. (1998). Laboratory-derived friction laws and their application to seismic faulting. *Annual Reviews of Earth and Planetary Science*, *26*, 643–696. https://doi.org/10.1146/annurev.earth.26.1.643

Marty, S., Passelègue, F. X., Aubry, J., Bhat, H. S., Schubnel, A., & Madariaga, R. (2019). Origin of high-frequency radiation during laboratory earthquakes. *Geophysical Research Letters*, *46*, 3755–3763. https://doi.org/10.1029/2018gl080519

Mayeda, K., Malagnini, L., & Walter, W. R. (2007). A new spectral ratio method using narrow band coda envelopes: Evidence for non-self-similarity in the Hector Mine. *Geophysical Research Letters*, *34*, L11303. https://doi.org/10.1029/2007GL030041

Mori, J., Abercrombie, R. E., & Kanamori, H. (2003). Stress drops and radiated energies of aftershocks of the 1994 Northridge, California, earthquake. *Journal of Geophysical Research*, *108*, 2545. https://doi.org/10.1029/2001JB000474

Mori, J., & Frankel, A. (1990). Source parameters for small events associated with the 1986 North Palm-Springs, California, earthquake determined using empirical Green-functions. *Bulletin of the Seismological Society of America*, *80*, 278–295. https://doi.org/10.1785/bssa0800030507

Nanometrics Seismological Instruments. (2013). *Nanometrics research network*. IFDSN.

Oklahoma Geological Survey. (1978). *Oklahoma seismic network*. IFDSN. https://doi.org/10.7914/SN/OK

Oth, A., Bindi, D., Parolai, S., & Di Giacomo, D. (2011). Spectral analysis of K-NET and KiK-net data in Japan, Part II: On attenuation characteristics, source spectra, and site response of borehole and surface stations. *Bulletin of the Seismological Society of America*, *101*, 667–687. https://doi.org/10.1785/0120100135

Parker, P. A., Baltay, A. S., Rekoske, J., & Thompson, E. M. (2020). Repeatable source, path, and site effects from the 2019 **M**M 7.1 Ridgecrest earthquake sequence, *Bulletin of the Seismological Society of America, 110* (4): 1530–1548. https://doi.org/10.1785/0120200008

Pennington, C., Chen, X., Abercrombie, R. W., & Wu, Q. (2021). Cross validation of stress drop estimates and interpretations for the 2011 Prague, OK, earthquake sequence using multiple methods. *Journal of Geophysical Research: Solid Earth*, *126*, e2020JB020888. https://doi.org/10.1029/2020JB020888

Prieto, G. A., Shearer, P. M., Vernon, F. L., & Kilb, D. (2004). Earthquake source scaling and self-similarity estimation from stacking P and S spectra. *Journal of Geophysical Research*, *109*, B08310. https://doi.org/10.1029/2004JB003084

Ross, Z. E., Kanamori, H., & Hauksson, E. (2017). Anomalously large complete stress drop during the 2016 M_w 5.2 Borrego Springs earthquake inferred by waveform modeling and near-source aftershock deficit. *Geophysical Research Letters*, *44*, 5994–6001. https://doi.org/10.1002/2017GL073338

Rubinstein, J. L., Ellsworth, W. L., & Dougherty, S. L. (2018). The 2013–2016 induced earthquakes in Harper and Sumner Counties, Southern Kansas. *Bulletin of the Seismological Society of America*, *108*(2), 674–689. https://doi.org/10.1785/0120170209

Ruhl, C. J., & Abercrombie, R. E. (2020). *Systematic fault plane analysis in complex earthquake sequences: Application to the 2019 Ridgecrest, CA and 2008 Mogul, NV earthquakes. Poster Presentation at 2020 SCEC Annual Meeting*.

Ruhl, C. J., Abercrombie, R. E., & Smith, K. D. (2017). Spatiotemporal variation of stress drop during the 2008 Mogul, Nevada, earthquake swarm. *Journal of Geophysical Research: Solid Earth*, *122*, 8163–8180. https://doi.org/10.1002/2017jb014601

Ruhl, C. J., Abercrombie, R. E., Smith, K. D., & Zaliapin, I. (2016). Complex spatiotemporal evolution of the 2008 *Mw* 4.9 Mogul earthquake swarm (Reno, Nevada): Interplay of fluid and faulting. *Journal of Geophysical Research: Solid Earth*, *121*, 8196–8216. https://doi.org/10.1002/2016JB013399

Scuderi, M. M., Marone, C., Tinti, E., Di Stefano, G., & Collettini, C. (2016). Precursory changes in seismic velocity for the spectrum of earthquake failure modes. *Nature Geoscience*, *9*(9), 695–700. https://doi.org/10.1038/ngeo2775

Shaw, J. H., Plesch, A., Tape, C., Suess, M. P., Jordan, T. H., Ely, G., et al. (2015). Unified structural representation of the southern California crust and upper mantle. *Earth and Planetary Science Letters*, *415*, 1–15. https://doi.org/10.1016/j.epsl.2015.01.016

Shearer, P. M., Abercrombie, R. E., Trugman, D. T., & Wang, W. (2019). Comparing EGF methods for estimating corner frequency and stress drop from P wave spectra. *Journal of Geophysical Research: Solid Earth*, *124*(4), 3966–3986. https://doi.org/10.1029/2018JB016957

Shearer, P. M., Prieto, G. A., & Hauksson, E. (2006). Comprehensive analysis of earthquake source spectra in Southern California. *Journal of Geophysical Research*, *111*, B06303. https://doi.org/10.1029/2005JB003979

Sibson, R. H. (1974). Frictional constraints on thrust, wrench and normal faults. *Nature*, *249*(5457), 542–544. https://doi.org/10.1038/249542a0

Small, P., Gill, D., Maechling, P. J., Taborda, R., Callaghan, S., Jordan, T. H., et al. (2017). The SCEC unified community velocity model software framework. *Seismological Research Letters*, *88*(5), 1539–1552. https://doi.org/10.1785/0220170082

Southern California Earthquake Data Center. (2013). Southern California Earthquake Center (SCEC), Caltech, Dataset. https://doi.org/10.7909/C3WD3xH1

Thurber, C., Zhang, H., Waldhauser, F., Hardebeck, J., Michael, A., & Eberhart-Phillips, D. (2006). Three-dimensional compressional wavespeed model, earthquake relocations, and focal mechanisms for the Parkfield, California, region. *Bulletin of the Seismological Society of America*, *96*(4B), 38–49. https://doi.org/10.1785/0120050825

Toth, C. R., Holland, A. A., Keranen, K. M., & Gibson, A. (2012). *Relocation and comparison of the 2010 M 4.1 and 2011 M 5.6 earthquake sequences in Lincoln County, Oklahoma. Eastern Section SSA 2012 Annual Meeting, Blacksburg, Virginia, 28–30 October 2012*.

Trugman, D. T. (2020). Stress-drop and source scaling of the 2019 Ridgecrest, California, earthquake sequence. *Bulletin of the Seismological Society of America*, *110*, 1859–1871. https://doi.org/10.1785/0120200009

Trugman, D. T., Dougherty, S. L., Cochran, E. S., & Shearer, P. M. (2017). Source spectral properties of small to moderate earthquakes in southern Kansas. *Journal of Geophysical Research: Solid Earth*, *122*, 8021–8034. https://doi.org/10.1002/2017JB014649

Trugman, D. T., & Savvaidis, A. (2021). Source spectral properties of earthquakes in the Delaware Basin of West Texas. *Seismological Research Letters*, *92*(4), 2477–2489. https://doi.org/10.1785/0220200461

Trugman, D. T., & Shearer, P. M. (2017). Application of an improved spectral decomposition method to examine earthquake source scaling in Southern California. *Journal of Geophysical Research: Solid Earth*, *122*, 2890–2910. https://doi.org/10.1002/2017JB013971

Trugman, D. T., & Shearer, P. M. (2018). Strong correlation between stress drop and peak ground acceleration for recent M 1–4 earthquakes in the San Francisco Bay Area. *Bulletin of the Seismological Society of America*, *108*(2), 929–945. https://doi.org/10.1785/0120170245

Voyles, J. R., Pitarka, A., Koper, K. D., & Holt, M. M. (2019).*Simulated effects of shallow crustal heterogeneity, surface topography, and seismic source depth on coda wave generation for magnitude-based depth discrimination, Abstract S11E-0417. Presented at Fall Meeting of the American Geophysical Union, Washington, DC, December 9–13*.

Walter, W. R., Yoo, S.-H., Mayeda, K., & Gök, R. (2017). Earthquake stress via event ratio levels: Application to the 2011 and 2016 Oklahoma seismic sequences. *Geophysical Research Letters*, *44*, 3147–3155. https://doi.org/10.1002/2016GL072348

Yoshimitsu, N., Ellsworth, W. L., & Beroza, G. C. (2019). Robust stress drop estimates of potentially induced earthquakes in Oklahoma: Evaluation of empirical Green's function. *Journal of Geophysical Research: Solid Earth*, *124*, 5854–5866. https://doi.org/10.1029/2019JB017483

Zhang, J., Chen, X., & Abercrombie, R. E. (2019). *Resolving the spatiotemporal variability of small earthquake source parameters at Parkfield and their relationship with 2004 M6 Parkfield earthquake, Abstract S51E-0445. Presented at 2019 Fall Meeting, AGU, San Francisco, CA, December 9–13*.

Zoback, M. D., & Harjes, H.-P. (1997). Injection-induced earthquakes and crustal stress at 9 km depth at the KTB deep drilling site, Germany. *Journal of Geophysical Research*, *102*(B8), 18477–18491. https://doi.org/10.1029/96JB02814